Dual-mode Nanophotonic Upconversion Oxygen Sensors

Esmaeil Heydari [a,b,*], Javad AmirAhmadi [a], Nahid Ghazyani [a], Gongxun Bai [c], Hossein Zare-Behtash [d], MohammadHossein MajlesAra [a,b]

Nanophotonic biosensors capable of being excited in the NIR spectrum have applications in various sectors. Here, we develop a 980 nm-excitable nanophotonic sensor for real-time oxygen detection in both water and air by analyzing the photoluminescent lifetime and intensity using a nanocomposite of lanthanide-doped $NaYF_4$:Yb^{3+}, Tm^{3+} upconversion nanoparticles, and a PtTFPP platinum porphyrin complex in a polystyrene matrix. Excellent overlap between the emission of the upconversion nanoparticles and the excitation band of the PtTFPP guarantees a 68 % efficient excitation of the PtTFPP molecules by a 980 nm NIR laser. For the first time, the oxygen sensitivity of the upconversion nanoparticles alone was reported, and it was demonstrated that the PL lifetime-based sensitivity slope was boosted more than 10-time by adding PtTFPP oxygen-sensitive molecules due to the energy transfer from the upconversion nano-emitters. In addition, the functionality of the upconversion-based sensor was investigated by analyzing its sensitivity, stability, reversibility, and temperature-dependent lifetime in both water and air, and its performance was compared with the sensor exposed to direct excitation at 410 nm. More importantly, the sensor was implanted under the skin of a chicken, and it was demonstrated that the PL intensity was amplified more than 12-time by employing the 980 nm excitation laser instead of 410 nm laser light. Therefore, excellent emission of the sensor under the skin paves the way for the development of implantable oxygen sensor platforms.

1. Introduction

A precise measurement of the oxygen level is necessary for various applications such as in medicine, biotechnology, food packaging, pharmaceutical industries, water waste treatment, aerospace, automotive, and aquaculture.[1] For decades, Clark electrodes, in the category of chemical oxygen sensors, have been used to measure instant dissolved-oxygen (DO) concentration. However, they suffer from major drawbacks such as oxygen consumption while measurement, which is detrimental in low-concentration detection, the requirement for repetitive calibration, regular replacement of the electrolyte solution, and the large electrode size, which is a challenge in some applications due to its intrusiveness. Recently, photonic/optical oxygen sensors have received much attention due to their non-invasive, rapid response, easy to miniaturize, low-cost, long-term calibration stability, and, most importantly, no oxygen consumption during measurements.[2, 3] In these sensors, the mechanism of oxygen detection is based on the quenching of photoluminescence (PL) intensity or lifetime due to the collision with oxygen (O_2) molecules present in the environment. Optical oxygen-sensitive probes (OSPs) based on ruthenium, platinum, and palladium complexes are commonly used to sense the oxygen concentration, where the O_2 molecules dynamically and reversely quench both the PL intensity and lifetime. The lifetime-based O_2 sensing, known as time-resolved PL spectroscopy, has superior advantages over the intensity-based measurement. Ideally, PL lifetime values are independent of the concentration, thickness, and photobleaching; in addition, signal drift is considerably less than in the intensity-based measurement, which results in more excellent stability. Since the lifetime-based measurement is immune to the intensity fluctuation and background emissions, it is a promising approach for O2 monitoring in living tissues and inhomogeneous environments.[4, 5] The OSP molecules are optically excited to a triplet energy state and consequently quenched via collisional interaction with surrounding O_2 molecules. Both PL intensity and lifetime are reduced during this process. The multi-site Stern-Volmer equation, describing the relationship between the variation in the PL intensity or lifetime with O_2 concentration, is provided in equation 1:

$$I_0/I = \tau_0/\tau = (\Sigma\, f_{0j} / 1+K_{SVj}[O_2])^{-1} \qquad (1)$$

where I and τ are the intensity and lifetime, I_0 and τ_0 are the intensity and lifetime at zero O_2 concentration, f_{0j} are fractional contributions to the unquenched steady-state emission at the monitoring wavelength[6], K_{SVj} are the Stern-Volmer constants, and $[O_2]$ is the concentration of O_2.[7-9] The excitation source of the OSPs is usually in the UV-VIS spectral range. However, this spectral range is detrimental for biological and medical applications due to the high energy levels. Instead, upconversion (UC) photoluminophores exhibit unique properties such as optical excitation with near-infrared (NIR) photons leading to a higher penetration depth in tissues in the order of 2.5 mm[10-12], minimum photobleaching, and photodegradation, sharp emission band, and lack of autofluorescence. In 2011, a composite of $NaYF_4$:Yb^{3+},Tm^{3+} UCNPs in iridium complex was used for intensity-based oxygen sensing in the air.[13] Lanthanide-doped upconversion nanoparticles (UCNPs) through a nonlinear process, absorb two or

[a] Faculty of Physics, Kharazmi University, Tehran, 15719-14911, Iran.
[b] Applied Science Research Center, Kharazmi University, Tehran, 15719-14911, Iran
[c] College of Optical and Electronic Technology, China Jiliang University, Hangzhou, 310018, China.
[d] James Watt School of Engineering, University of Glasgow, Glasgow G12 8QQ, UK. *Corresponding author: e.heydari@khu.ac.ir
Electronic Supplementary Information (ESI) available: [details of any supplementary information available should be included here]. See DOI: 10.1039/x0xx00000x

more low-energy NIR photons and convert them to a high-energy photon. UCNPs' PL begins with an excitation power less than 1 W, which is quite low among nonlinear materials and is one of the reasons for the scientific interest in these nanomaterials. Ln^{3+} ions with unique optical properties such as abundant 4f energy levels, excellent photostability, long lifetime, large anti-Stokes shift, and narrow emission bands have been the focus of many researchers.[14-18] As a result, lanthanide-doped UCNPs have found a wide range of potential applications in the biomedical, drug delivery and discovery, novel optical sensors [19-21], non-invasive optical imaging, anti-counterfeiting tags, and photovoltaics. [22-26] Unlike quantum dots (QD) and organic dyes, lanthanide-doped UCNPs' emissions are independent of their size or surrounding media.[27] The ground-state electron configuration of all lanthanide elements is in intra-4f orbitals, which is isolated by the 5s, 5p, and 6s shells. This configuration makes them photostable, and their photoluminescence is independent of their size and environmental factors. The 4f-4f transition is forbidden for the free lanthanide ions. However, it is partially allowed when they are doped into a host matrix due to the non-negligible dopant-host coupling effect [28-30], which is the reason behind their sharp emission spectrum. In general, Ln^{3+}-doped UCNPs comprise three components of an optically neutral host matrix, an Ln^{3+} ion as an activator, and another Ln^{3+} ion as a sensitizer. The Ln^{3+} ions are doped as a guest in the host matrix. Different host matrices exhibit different optical and physical properties.[31] Excitation energy transfer takes place when energy is transferred from a donor (D) in the excited state to an acceptor (A) in the ground state. Energy transfer occurs in both radiative and non-radiative forms. In the process of radiative energy transfer, a photon is emitted from the D ions and absorbed by the A ions. However, in the case of the non-radiative energy transfer processes, no photon is emitted during the energy transfer between D and A ions. In general, the energy-transfer efficiency of non-radiative processes can be higher.[32] The photon UC mechanism is usually divided into several general categories: excited-state absorption (ESA), energy transfer upconversion (ETU), photon avalanche (PA), cooperative sensitization upconversion (CSU), and cross-relaxation (CR). One or more of these mechanisms may occur simultaneously.[33] The dominant process in $NaYF_4$:Yb^{3+},Tm^{3+} is ETU.[34]

In this paper, we developed a 980 nm-excitable nanophotonic oxygen sensor based on a composite of $NaYF_4$:Yb^{3+}, Tm^{3+} lanthanide-doped UCNPs, and a platinum meso-tetra (pentafluorophenyl) porphyrin (PtTFPP) in a polystyrene (PS) matrix. This nanophotonic sensor is implemented for real-time and contactless oxygen detection using 980 nm NIR laser light, based on the analysis of both PL lifetime and intensity in both water and air. The sensor functionally is investigated through a comprehensive evaluation of the work function, stability, reversibility, and temperature-dependent sensitivity in the intensity and lifetime regimes in both water and air media using NIR and UV light sources. In addition, the crucial role of the 980 nm excitation photon is demonstrated by implanting the sensor under the skin of a chicken model and comparing the PL signal.

2. Materials and methods

2.1 Preparation of the UC OSP

Platinum meso-tetra (pentafluorophenyl) porphyrin, known as PtTFPP, from Frontier-Scientific, polystyrene (PS) polymer from Sigma-Aldrich, and toluene solvent (99.9%) was purchased from Merck. The $NaYF_4$:Yb^{3+}, Tm^{3+} UCNPs were synthesized using the hydrothermal method. A solution was prepared by dissolving 2 mg of PtTFPP in 500 µL of toluene. The solution was thoroughly mixed using a magnetic stirrer for 1 h. 0.1 g of PS matrix was dissolved in 500 µL of toluene and stirred at room temperature for 2 h to become completely uniform. Afterward, 5 µL of 38 mg/mL colloidal UCNPs in toluene was mixed with 25 µL of PtTFPP solution and 50 µL of PS solution. The mixture was cast onto a glass slide and annealed for 15 min at 60 °C to form a 100 µm thick disk. Similarly, a UCNPs-PS sample alone without PtTFPP OSP was prepared.

2.2 Instrumentation

A Thorlabs CCS100 spectrometer was used for the PL spectral analysis. Analytik Jena Specord 210 Plus was used to measure the absorption spectra. An Ophir Nova II power meter was used to measure the excitation laser beam power. 980 nm and 410 nm laser diodes from CNI (MDL-III) were used as excitation sources. The 980 nm laser power was tuned to 300 mW for the intensity-based measurement and 2 W for the lifetime-based measurement in the entire experiment. The 410 nm laser power was 5 mW for the intensity-based measurement and 10 mW for the lifetime-based measurement. Zeiss EM900 was used to measure the TEM image of the UCNPs. Lutron YK-22DOA O2 meters were employed to measure the O_2 in the air. A HANNA HI-2040 O2 meter was used to measure DO in water. A DG535 Digital Delay generator from Stanford Research Systems was employed to tune the pulse width and duration of the lasers. The pulse duration and width of the excitation lasers in the PL lifetime measurement were 1 Hz and 3 ms, respectively. A PDB210A/M Thorlabs photodetector was used to detect PL lifetime and Keysight U2702A USB oscilloscope for data acquisition. XRD pattern was measured using Philips PW1730 x-ray diffractometer.

3. Results and discussion

The nanocomposite comprises the PtTFPP complex as the OSP, and NIR-excitable $NaYF_4$:Yb^{3+}, Tm^{3+} UCNPs were prepared as UC OSP. First, the PL and absorption spectra of the UC OSP were characterized. Excellent spectral overlap between the PL of the UCNPs and absorption spectra of the OSP is required for the optimum energy transfer between the PtTFPP molecules and UCNPs. The

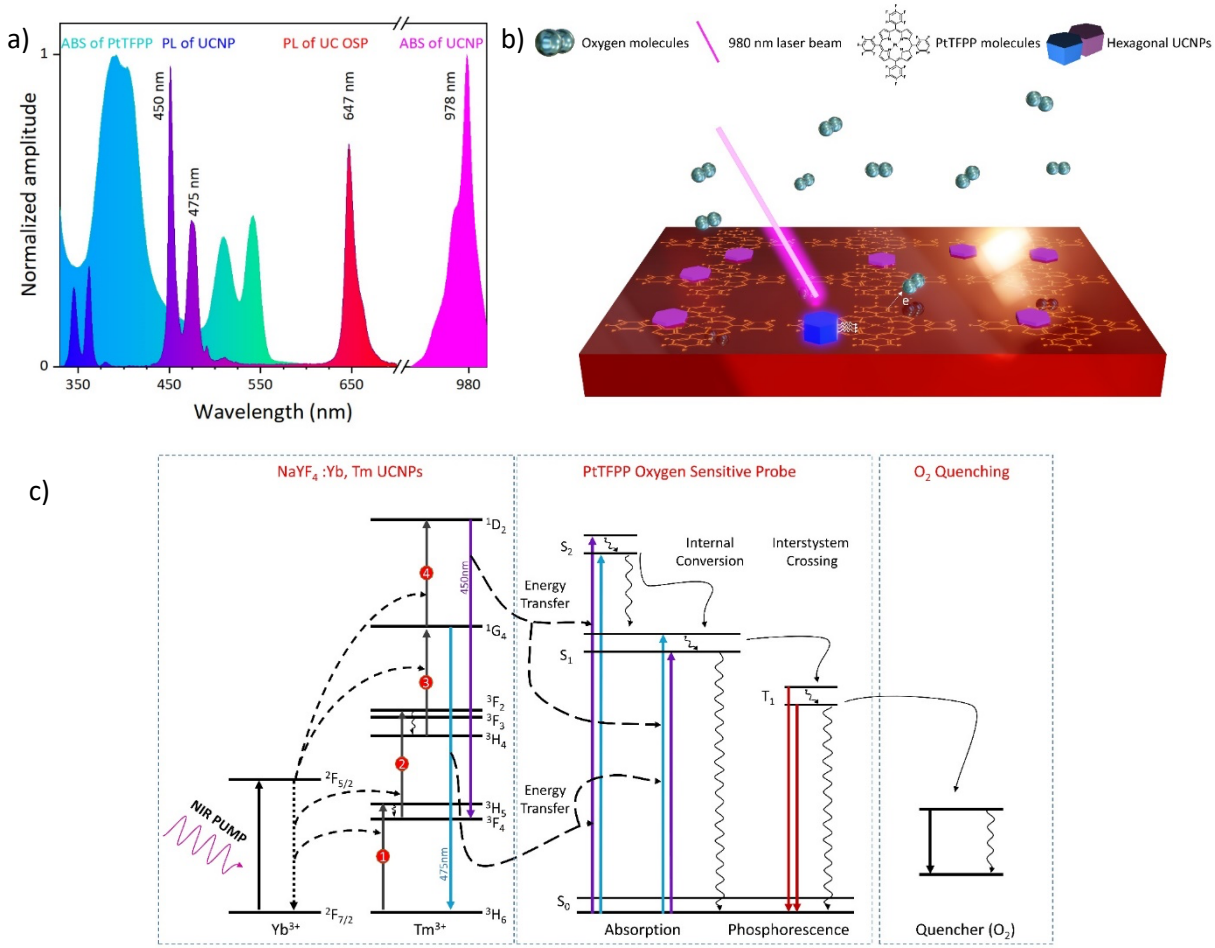

Fig. 1 Concept and mechanism of the UC OSP (a) Absorption and PL spectra of PtTFPP-UCNP-PS OSP. The pink band is the UCNPs absorption spectrum. The red band is the PtTFPP-UCNP-PS OSP PL spectrum; the blue-green band is the PtTFPP absorption spectrum. (b) Schematic of UC OSP principle based on a nanocomposite of $NaYF_4$:Yb^{3+}, Tm^{3+} NPs in the PtTFPP-PS matrix. (c) Energy diagram for energy transfer between $NaYF_4$: Yb, Tm UCNPs, PtTFPP-PS OSP, and the O_2 molecules.

UCNPs spectrum has two dominant peaks in the blue spectrum, which were used for the excitation of the PtTFPP molecules. (Fig. 1a) depicts the absorption spectrum of the PtTFPP OSP in a blue-green color, which has peaks at 390 nm, 512 nm, and 542 nm. The absorbance maximum of UCNPs is at 978 nm, shown with a pink color in (Fig. 1a) Thus, a 980 nm laser was used to excite the UCNPs. The UCNPs exhibit narrow visible emission bands at 450 nm and 475 nm, shown in blue. The peak at 450 nm corresponds to the 4-photon processes from the $^1D_2$ state to the $^3F_4$ state in Tm^{3+} ions, and the peak at 475 nm corresponds to the 3-photon processes from the $^1G_4$ state to the $^3H_6$ and $^3F_4$ states in the Tm^{3+} ions. The UC OSP (PtTFPP-UCNPS-PS) was prepared by doping the UCNP in a PtTFPP-Polystyrene (PS) solution. When it was excited by a 980 nm laser, the corresponding PL exhibited a red emission maximum at 647 nm. According to (Fig. 1a) there is an excellent overlap between the blue emissions of the UCNPs and the absorption spectrum of the PtTFPP molecules, enabling the NIR excitation of the UC OSP by a 980 nm excitation laser. This overlap is a prerequisite for energy transfer between the UCNPs and PtTFPP OSP. In addition, the distance between the donor UCNPs and acceptor OSP is important, which can be tuned by selecting an appropriate solvent and host matrix. This energy transfer occurs at distances below 20 nm, and is called Förster resonance energy transfer (FRET) or luminescence resonance energy transfer (LRET).[35-39] The PS matrix supported the required oxygen permeability and provided an excellent emission signal, and therefore, was chosen as the host matrix. The emission spectra of the UC OSP were recorded when excited by the 980 nm laser, which is shown with the red spectrum in the (Fig. 1a) The general concept of the UC OSP is depicted in (Fig. 1b) It reveals the processes of UCNPs excitation, energy transfer, PtTFPP radiation, and phosphorescence quenching by oxygen molecules. At first, the UCNPs absorb the 980 nm photons and act as nano-emitters to transfer the energy to the OSP molecules. Thus, the blue emission of UCNPs is absorbed by the PtTFPP molecules and subsequently, the excited molecules are relaxed back by phosphorescence emission. Finally, the emission of the excited PtTFPP molecules is quenched in the presence of the O_2 molecules and the corresponding intensity and lifetime are reduced. (Fig. 1c) shows the energy transfer between lanthanide-doped UCNPs and the PtTFPP OSP. Yb^{3+} ions, as the sensitizer in $NaYF_4$:Yb^{3+}, Tm^{3+} UCNPs, absorb the NIR photons through the $^2F_{7/2}$ to $^2F_{5/2}$ transition. Afterward, the energy is transferred to the Tm ions as activators. Thus, the energy of 450 nm and 475 nm emission peaks,

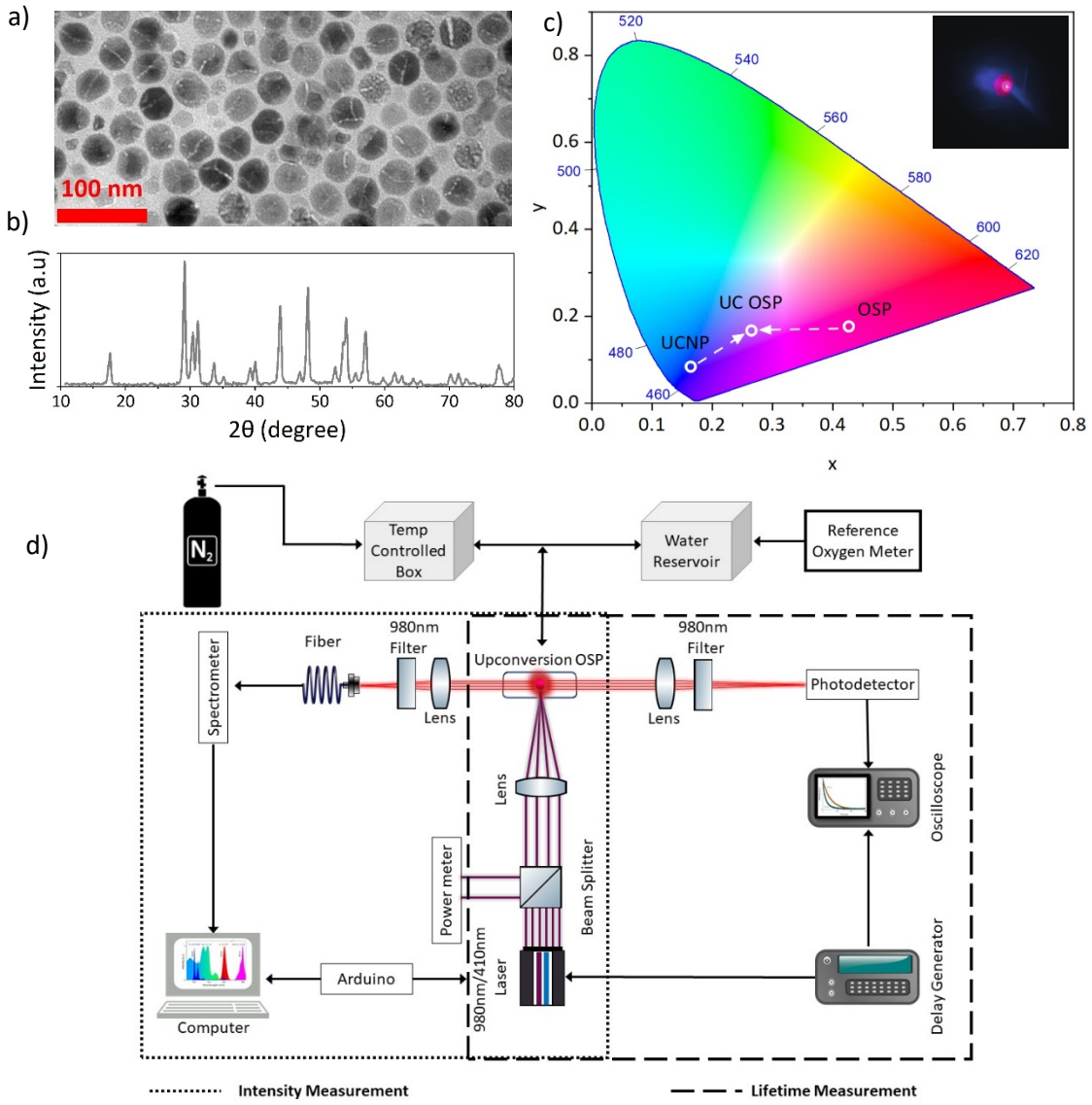

Fig. 2 UCNPs and the optical setup for the OSP characterization (a) TEM image of the UCNPs with an average size of 50 nm. (b) XRD pattern of the UCNPs. (c) CIE1931 chromaticity diagram of UCNPs, PtTFPP complex, and the UC OSP. Inset is the emission of the excited UC OSP. (d) The optical setup was used for the intensity (dotted-line) and lifetime (large dashed-line) measurement.

corresponding to $^1D_2$ to $^3F_4$ and $^1G_4$ to $^3H_6$ transitions, are transferred to the ground state (S_0) of PtTFPP molecules due to the overlap of the UCNP's PL and PtTFPP absorption spectra. Therefore, the energy of excited molecules is transferred to the lowest excited state S_1 through internal conversion before intersystem crossing to the triplet T_1. In the case of radiative intersystem crossing and then transferred from the T_1 electronic state to the Si state. In the presence of O_2 molecules, the PtTFPP phosphorescence emission is dynamically quenched by non-radiative interaction between the O_2 and PtTFPP molecules.[40] In (Fig. 2a) a TEM image of the UCNPs is presented with an average size of 50 nm. (Fig. 2b) shows the typical XRD pattern of the $NaYF_4$;Yb^{3+},Tm^{3+} where the diffraction peaks demonstrate the co-existence of cubic and hexagonal phases[41-45]. The CIE1931 chromaticity diagram of each component and the final UC OSP are displayed in (Fig. 2c) This diagram shows the color coordinates of the emissions. The color of the UCNPs is in a blue coordinate $[0.16\,,0.08]$, PtTFPP in a red coordinate $[0.42\,,0.17]$ and their combination is in a pink color coordinate $[0.26\,,0.16]$ In the simultaneous phosphorescence emission, the emission color is transferred to the intermediate of these two colors. The top right inset shows the emission color of the UC OSP excited by 980 nm laser light. (Fig. 2d) shows the optical setup used for the lifetime and intensity-based measurement. The 410 nm and 980 nm lasers were used for direct and indirect excitation of the UC OSP, respectively. The 410 nm laser was used as a reference to evaluate the function of the 980 nm excited UC OSP. In the intensity-based setup indicated with the dotted lines, the laser beam was separated

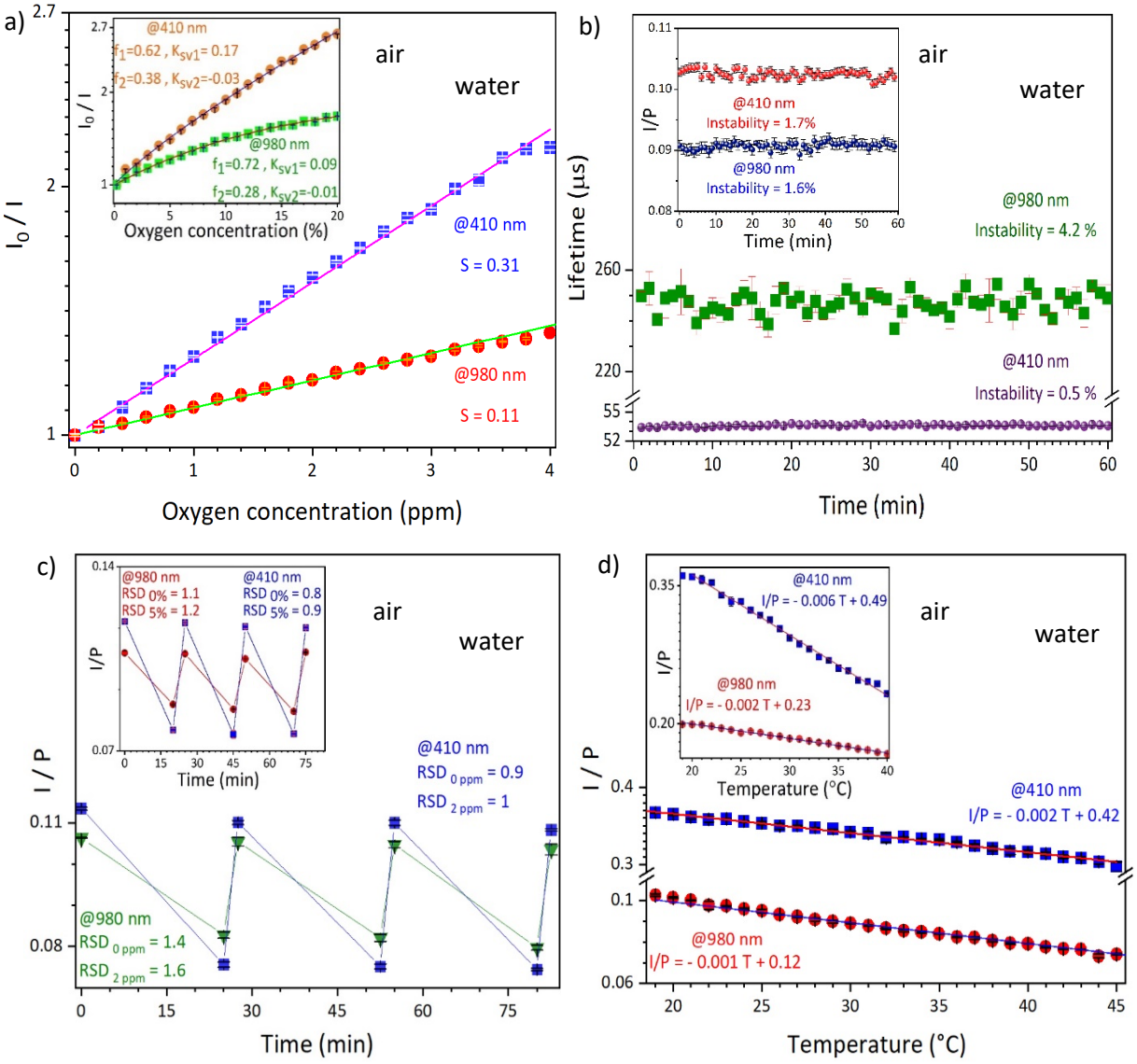

Fig. 3 Intensity-based characterization of the UC OSP (a) I/I_0 Stern-Volmer diagram shows the sensor work function in the water with direct laser excitation at 410 nm laser (blue squares) and indirect NIR excitation with a 980 nm laser (red circles). Inset shows intensity ratio versus concentration of oxygen in the air. Orange circles represent excitation by the 410 nm, and green squares excitation with the 980 nm laser. (b) The green and violet diagram shows the stability of UC OSP excited by the 410 nm and 980 nm laser light in the water. Red circles and dark blue circles in the inset show the stability for the excitation with 410 nm and 980 nm in the air. (c) Reversibility of UC OSP when the DO was changed between 0.0 and 2.0 ppm. Blue squares correspond to the 410 nm excitation photons and green triangles to the 980 nm photons. Inset shows the reversibility in the air for the variation between 0.0 % and 5.0 % O2 concentration .Red circles represent excitation with the 980 nm photons and blue squares excitation with the 410 nm photons. (d) Intensity variation in terms of temperature is linear. The inset shows the intensity variation based on the temperature in the air, where the blue squares and red circles were excited with the 410 nm and 980 nm photons, respectively.

by a beam splitter into two parts to monitor the excitation laser power continuously. The laser beam was then focused on the UC OSP, and its PL emission was collected onto the fiber optic cable connected to a Thorlabs optical spectrometer. A 980 nm filter is placed in front of the optical fiber to prevent the 980 nm laser light entrance to the spectrometer. An Arduino UNO in combination with LabVIEW was used for the spectrometer data acquisition and controlling the laser (switch on the lasers for 10 s and off for 60 s). A delay generator was used to generate 3 ms laser pulses in the lifetime-based setup. The UC OSP was excited by the lasers, and the PL emission was collected onto a Thorlabs Si amplified photodetector. The photodetector was connected to an Agilent digital oscilloscope, which was externally triggered by the delay generator. A water reservoir, an in-house developed temperature-controlled chamber, and N_2 gas were used to control the temperature and O_2 concentration in the experiments. Therefore, the UC OSP was placed inside a plexiglass chamber to investigate its work function and sensitivity. The chamber had an inlet to supply the N_2 gas, a HANNA Edge, and Lutron reference O_2 sensors for monitoring the DO concentration in water and O_2 percentage in air, respectively.

3.1 PL intensity-based measurements

PL intensity and lifetime of the UC OSP change for different concentrations of O_2 in water and air. I_0/I Stern-Volmer diagrams for the excitation with the 410 nm UV and 980 nm NI laser beams in water are plotted in (Fig. 3a) This illustrates the change in the ratio of zero O_2 intensity to any deliberate O_2 PL intensity I_0/I for different concentrations of DO in the water. Blue squares correspond to the excitation with the 410 nm laser light and the red circles to the excitation with the 980 nm laser. The UC OSP was placed inside a plexiglass chamber equipped with an inlet and outlet. The water was continuously and steadily pumped into the chamber from a sealed water reservoir where the O_2 concentration and temperature were controlled. A stream of N_2 gas was injected into the water reservoir until the concentration of DO reached 0.0 ppm. Then, the intensity was measured for different O_2 concentrations ranging from 0.0 ppm to 4.0 ppm. The excitation power of 410 nm and 980 nm lasers were tuned to 5 mW and 300 mW, respectively. The temperature was maintained at 25.0 ± 0.2 °C in both experiments using a closed-loop temperature controller. The results demonstrate that the behavior of the Stern-Volmer diagram is linear in the oxygen range of 0.0 ppm to 4.0 ppm in such a way that the sensitivity slope of the UC OSP excited by 980 nm laser light is 0.11 and when it was excited by 410 nm laser light is 0.31. Therefore, the O_2 sensitivity of the UC OSP is higher when it is directly excited by the 410 nm laser light. This is attributed to the higher number of excited OSP molecules available to interact with the O_2 molecules. (Fig. 3a inset) shows the O_2 sensitivity of the UC OSP in air. The orange circles correspond to the excitation with the 410 nm photons, and the green squares correspond to the 980 nm NIR excitation. In this case, the N_2 gas was injected into the measurement chamber for the UC OSP calibration in the air until the O_2 concentration reached zero percent, monitored by the reference oxygen meter. Afterward, the N_2 injection was stopped, and the intensity was recorded for O_2 in the range of 0.0 % to 20.9 %. Each point represents an average value of three consequent measurements. Inset shows the sensitivity for the 410 nm excitation is again higher than the 980 nm excitation. Hence, for O_2 measurements in air and water, it is possible to employ the NI-excited UC OSP however the O_2 sensitivity of the UC OSP is reduced when it is excited by the 980 nm photons due to a reduction in the overall quantum yield of the UC OSP and interaction with the O_2 molecules. The characteristics of UC OSP are specified by parameters such as stability, reversibility, and operating range. The instability of the sensor is the amount of deviation relative to the mean value therefore the lower the signal drift, the higher stable and accurate the sensor [46, 47]. The UC OSP stability test was performed in the water chamber where the temperature and the O_2 level were controlled. In (Fig. 3b) the ratio of the PL intensity (I) to the excitation laser power (P) is plotted over a 60 min period. The change in the excitation laser power was small (less than one percent) however a ratiometric measurement was performed to reduce the corresponding error. Thus, the UC OSP emission intensity was divided by the laser power. It shows that the PL instability for the two excitation lasers of 410 nm (green squares) and 980 nm (purple stars) in the water are 4.6 % and 2.6 %, respectively. It was observed that the signal level decreases during this test which is attributed to photobleaching. (Fig. 3b inset) shows the results of the stability evaluation in the air in which the instability for the excitation at the 410 nm (red circles) and 980 nm (blue circles) are 1.7 % and 1.6 %, respectively. Measurements carried out in air exhibit higher PL intensities and stabilities because the signal-to-noise ratio increases, and therefore the measurement error is decreased. Another important parameter of the UC OSP is reversibility. The reversibility of the sensor was obtained by calculating the relative standard deviation (RSD) parameter. The RSD is a statistical quantity known as the coefficient of variance. (Fig. 3c) shows the reversibility of the UC OSP where the DO concentration was modulated between 0.0 ppm and 2.0 ppm for the two excitation lasers, and the changes in the intensity ratio were recorded. The RSD values at 0.0 ppm and 2.0 ppm were 0.9 % and 1.0 % for the 410 nm photons (blue squares) and 1.4 % and 1.6 % for the 980 nm photons (green triangles) in water, respectively. (Fig. 3c inset) illustrates the reversibility results in the air where the RSD values at 0.0 % and 5.0 % O2 concentration were 0.8 % and 0.9 % for 410 nm photons (blue squares) and 1.1 % and 1.2 % for 980 nm photons (red circles), respectively. The reversibility of the UC OSP did not change significantly. In general, the lower the O_2 concentration, the higher the PL intensity of the UC OSP radiation, leading to a higher signal-to-noise ratio. This is why the RSD values are higher for lower O_2 concentrations. Typically, the PL intensity of metal-organic complexes is a function of the temperature. However, the intensity of UCNPs does not depend on the temperature. [48] Therefore, the response of the UC OSP for different temperatures is required to be investigated. The PL intensity was measured for a temperature range of 19.0 °C to 45.0 °C to achieve its corresponding work function. (Fig. 3d) depicts the PL intensity as a function of temperature when excited by 410 nm and 980 nm laser beams in the water chamber while the DO concentration was maintained at 0.0 %. The PL of the UC OSP shows a linear response with the temperature variation for both of the excitation wavelengths in such a way that the intensity to power ratio was reduced by increasing the temperature. The slopes of the temperature deviation are -0.002 and -0.001 for the 410 nm (blue squares) and 980 nm (red circles) excitation photons, respectively. (Fig. 3d inset) shows a similar experiment repeated in the air. Again, the intensity to power ratio linearly decreases with the slopes of -0.006 and -0.002 for the excitation with the 410 nm (blue squares) and 980 nm (red circles) photons, respectively. Therefore, UC OSP is less susceptible to temperature variations in both water and air when they are excited with 980 nm photons which are believed to be due to the involvement of the temperature-independent $NaYF_4:Yb^{3+}$, Tm^{3+} UCNPs in the emission process. In addition, the slope increased in the air due to the higher level of interaction with the O_2 molecules compared to the water case.

3.2 PL lifetime-based measurements

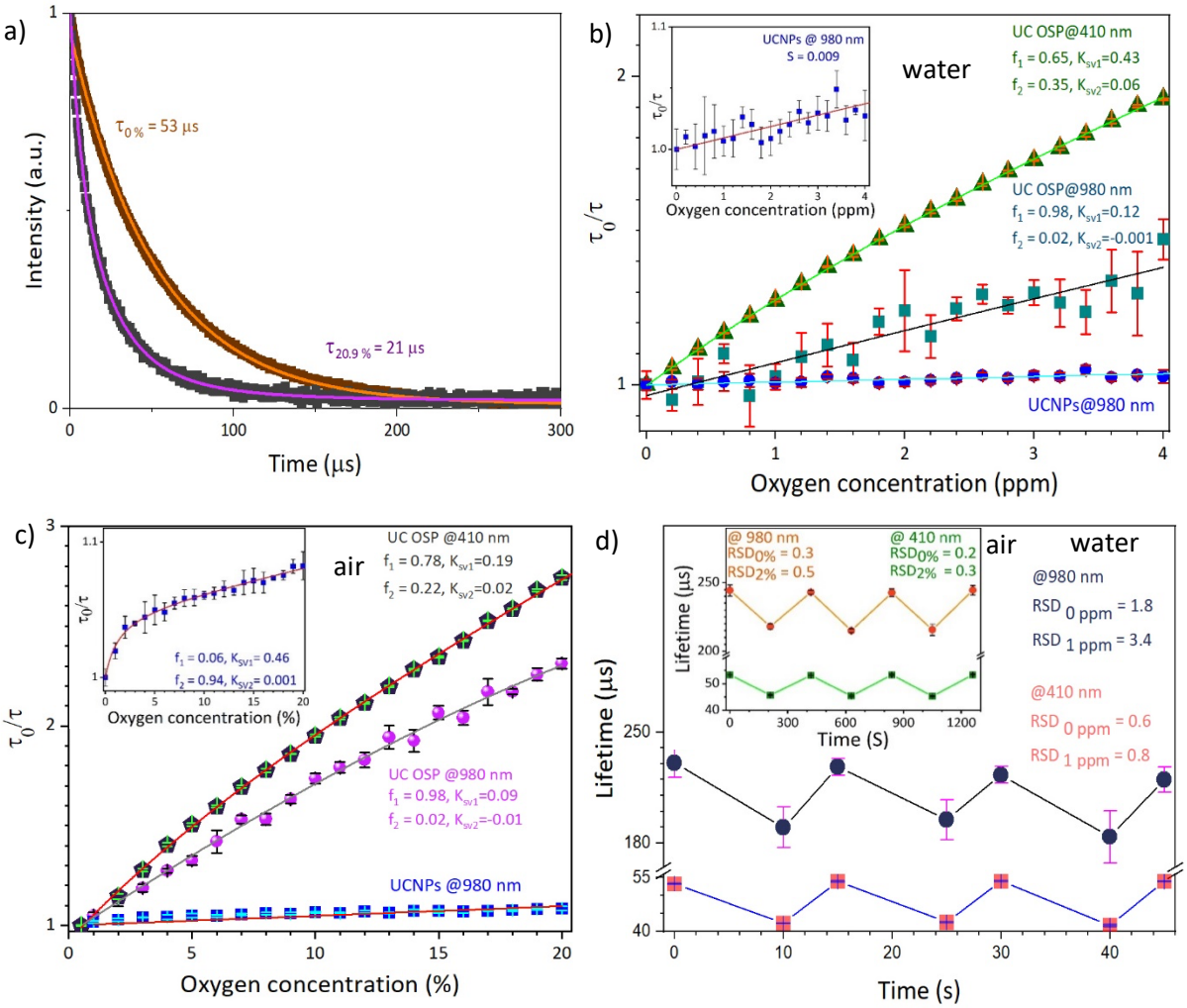

Fig. 4 Lifetime-based characterization of the UC OSP (a) PL lifetime of PtTFPP -PS excited with the 410 nm photons for 0.0 % (brown) and 20.9 % (purple) O_2 percentage in the air. (b) Stern-Volmer diagram for lifetime ratio as a function of the O_2 concentration in the water for the UCNPs-PS (blue circles), indirectly-excited (green squares) and directly-excited (green triangles) UC OSP. Inset is the magnified Stern-Volmer diagram of the UCNPs-PS. (c) Stern-Volmer diagram of τ_0/τ versus O_2 concentration of UCNPs-PS (blue squares), indirectly excited UC OSP (pink circles), and directly-excited UC OSP (black pentagonals) in air. Inset shows the magnified Stern-Volmer diagram for UCNPs-PS in the air. (d) Reversibility of the UC OSP for 410 nm (red square) and 980 nm (black circles) excitation photons in the water between 0.0 ppm and 1.0 ppm DO concentration. Inset shows the reversibility for the 410 nm (green squares) and 980 nm (orange circles) excitation photons in the air between 0.0 % and 2.0 % O_2 concentration.

Measurement of the PL lifetime of the UC OSP is the most reliable method for evaluating the O_2 concentration due to the effect of the photobleaching in intensity-based measurements. In addition, measurement of the UCNPs, PtTFPP, and UC OSP lifetimes enables the calculation of the energy transfer efficiency. (Fig. 4a) presents the time-resolved PL spectroscopy of PtTFPP-PS directly excited by the 410 nm laser beam for two O_2 concentrations of 20.9 % and 0.0 %, which correspond to approximate PL lifetimes of 21 µs (purple) and 53 µs (brown), respectively. The PL lifetime of the UCNPs in the PS matrix was measured as 331 ± 1 µs at the 20.9 % O_2 concertation and a temperature of 23.0 °C. The efficiency of the energy transfer was calculated using equation (2) [49],

$$E = 1 - \tau_{UC\ OSP} / \tau_{UC} \qquad (2)$$

where τ_{UC} and τ_{UC} OSP are the PL lifetime of $NaYF_4$:Yb^{3+}, Tm^{3+} without and with the PtTFPP OSP, respectively. Next, the lifetime of the UC OSP at the O_2 concentration of 20.9 % and the temperature of 23.0 °C in the air was measured as 106 ± 4 µs. The efficiency of energy transfer from the UCNP to the PtTFPP OSP was approximately 68 %. The described lifetime setup was used to obtain the work function of the UC OSP by applying different O_2 concentrations. (Fig. 4b) illustrates the Stern-Volmer diagram for the PL lifetime ratio as a function of the DO concentration in water, for UCNPs-PS (blue circles), UC OSP excited by 410 nm (light green), and UC OSP excited by 980 nm (dark green) photons fitted with one or two-site Stern-Volmer equations. It was observed that the lifetime ratio increased by increasing the DO concentration in water with different sensitivity slopes. The sensitivity slope was boosted from 0.009 for UCNPs-PS to 0.1 for UC OSP by applying the PtTFPP molecules, and the slope for direct excitation with 410 nm was 0.24. (Fig. 4c) shows the sensitivity slopes for UCNPs-PS (blue squares), 410 nm-excited UC OSP (black pentagonal), and 980 nm-excited UC OSP (pink circles) in air. The sensitivity slope increases from 0.005 for UCNPs to 0.06 for indirectly excited UC

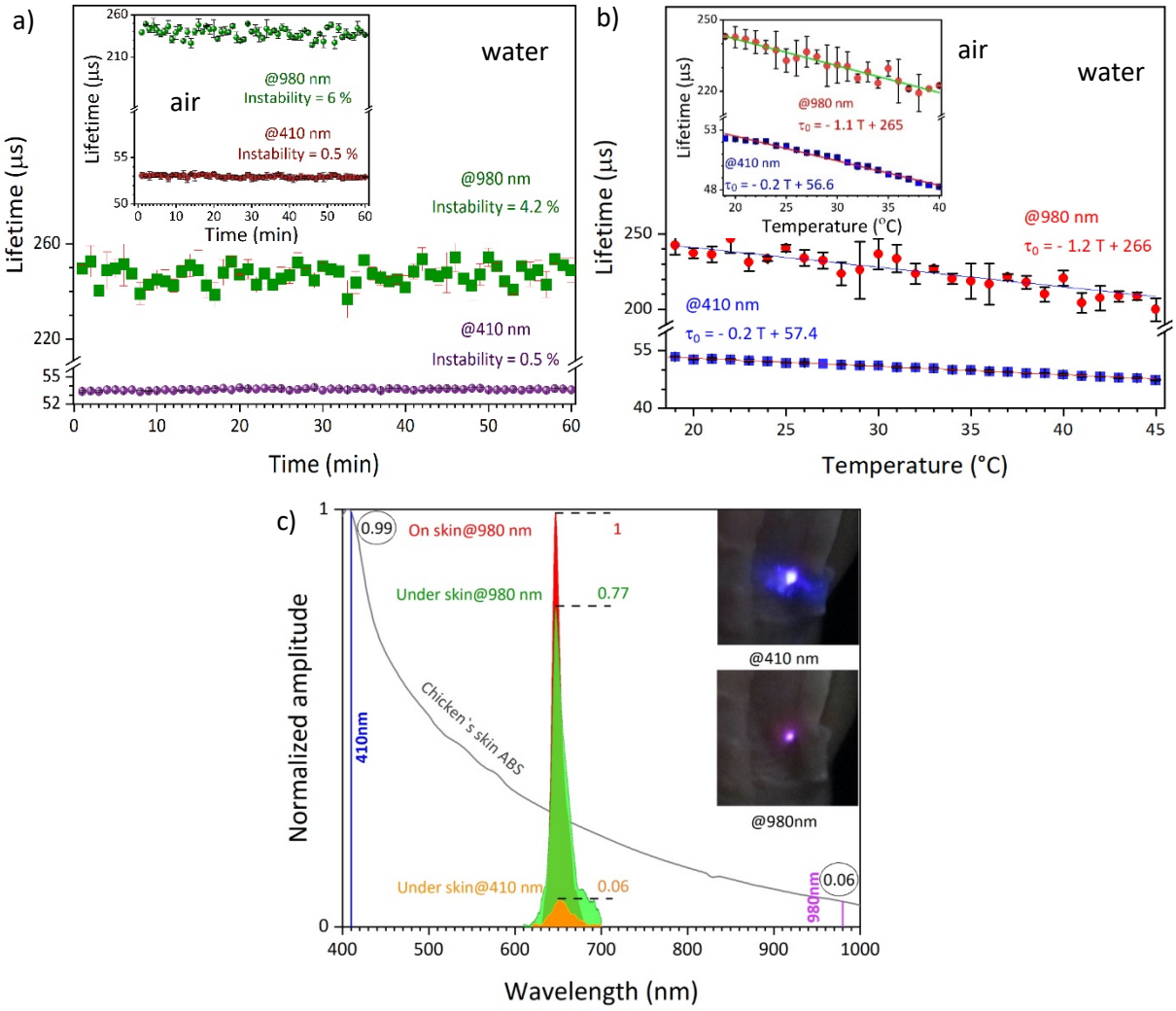

Fig .5 Stability and temperature dependency of the UC OSP (a) The lifetime stability of the UC OSP sensor in water and air (inset), which are excited by 980 nm (green) and 410 nm (purple) lasers. (b) It shows the temperature-dependent lifetime variation. Blue square and red circle represent the excitation with the 410 nm and 980 nm photon, respectively. The inset shows the temperature-dependent lifetime in the air. (c) Chicken skin absorption spectrum is shown with a black line, PL spectrum of the UC OSP on the skin excited at 980 nm in red, UC OSP implanted under the skin excited at 980 nm in green, and implanted sensor excited at 410 nm in orange. Inset top image corresponds to the excitation of the implanted UC OSP with 410 nm laser light where a blue scattered light was dominantly observed instead of a red emission. The bottom image corresponds to the excitation of the implanted UC OSP with 980 nm laser light where clearly an intense red emission was observed which was verified by the recorded absorption and PL spectra.

OSP. The sensitivity slope for the directly-excited UC OSP is 0.09. The slopes in the lifetime and intensity-based measurement must be equally based on the Stern-Volmer equation, and the observed minor difference is mostly attributed to the PL quenching affecting the intensity-based measurements. Most importantly, comparing the sensitivity slope of the UCNPs-PS and the UC OSP again demonstrates the energy transfer among them and emphasizes the role of the PtTFPP in boosting the O_2 sensitivity of the UC OSP. (Fig. 4c inset) depicts the magnified UCNPs-PS sensitivity diagram fitted with two-site Stern-Volmer equation. (Fig. 4d) showed the reversibility for the lifetime-based measurement when the UC OSP was excited using the 410 nm (black circles) and 980 nm (red squares) photons in water. Similar to the intensity-based measurement, the DO concentration was modulated several times between 0.0 ppm and 1.0 ppm. The corresponding RSD values were measured as 1.8 % and 3.4 % for the 980 nm excitation laser, and 0.6 % and 0.8 % for the 410 nm excitation laser, respectively. (Fig. 4d inset) demonstrates the reversibility by varying the O2 concentration from 0.0 % to 2.0 %, where the corresponding RSD values were 0.2 % and 0.3 % for the 410 nm (green squares) laser and 0.3 % and 0.5 % for the 980 nm laser (red circles) in the air, respectively. The results show again that the RSD value is lower for the lower O_2 concentration due to a higher signal-to-noise ratio.

(Fig. 5a) shows the lifetime stability of the UC OSP in water to evaluate its long-term performance where the DO concentration was kept at 0.0 ppm, and the temperature was maintained at 25.0 ± 0.1 °C. The instability for 410 nm and 980 nm excitations were 0.5 % (purple circles) and 4.2 % (green squares), respectively. (Fig. 5a inset) depicts the instability in the air for excitations at 410 nm and 980 nm with corresponding stabilities of 0.5 % (brown squares) and 6.0 % (green circles), respectively. In addition, the effect of the temperature on the lifetime of the UC OSP was investigated by changing the temperature from 19.0 °C to 45.0 °C while the DO concentration was maintained at 0.0 ppm. (Fig. 5b) demonstrates linear behaviours of the lifetime with a slope of -

0.2 for the 410 nm laser light (blue squares) and -1.2 for the excitation with the 980 nm laser light (red circles) in the water. (Fig. 5b inset) shows the slope is -0.2 for the 410 nm laser light (blue squares) and -1.1 for the excitation with the 980 nm photons (red circles) in air. The PL lifetime reduces with increasing temperature due to faster collisional relaxation and it was more susceptible to temperature variations when it was excited by 980 nm than 410 nm photons due to their effect on the Förster resonance energy transfer between the UCNPs and PtTFPP OSP. [50] This data is necessary to account for the temperature compensation for the calibration of the UC OSP. Then, the UC OSP was implanted under the skin of a chopped chicken in order to present a perspective of its potential applications where excitation wavelength plays a crucial role. (Fig. 5c) demonstrates the normalized absorption spectrum of the skin in black where it decreases from 0.99 at 410 nm to 0.06 at 980 nm. Therefore, the absorbance of the skin was reduced by 16.5-time by shifting from UV to NIR excitation wavelengths. In addition, the PL intensity of the implanted UC OSP was compared with the UC OSP placed on the skin for both 410 nm and 980 nm excitations to realize the potential benefits that this technology can bring to implantable sensors. The orange area is corresponding to the PL spectrum of the implanted UC OSP with an amplitude of 0.06 excited with 410 nm laser light. The green area is corresponding to the excitation with 980 nm laser light with an amplitude of 0.77. The red spectrum is the normalized PL of the UC OSP located on the skin. Interestingly, the PL signal was amplified 12.8-time by using UC nanotechnology. (Fig. 5c top inset) image shows the 410 nm-excited area on the skin. In this case, scattered UV laser light is dominated, and the emission cannot be recognized since the penetration depth of the UV light is very limited and mostly absorbed, therefore only a small fraction of the incident light excited the UC OSP. (Fig. 5c bottom inset) image depicts the PL emission of the implanted sensor, and in this case, the red PL emission can be clearly observed due to longer penetration depth and minor absorption. These observations are compatible with the measured absorption and emission spectra. Therefore, compared to an earlier report by Achatz, not only the characterization was performed in different media of air and water using time-resolved phosphorescence spectroscopy besides intensity-based measurement, a complete characterization of the UC OSP including the sensitivity, stability, reversibility, and temperature-dependent lifetime was carried out in two excitation wavelengths, and it was demonstrated the UCNPs alone could be used as oxygen sensors. In addition, the outstanding benefits of the 980 nm excitation were shown by implanting the UC OSP under the skin of a chicken model.

4. Conclusions

A 980 nm-excitable oxygen sensor has been developed by doping the $NaYF_4$:Yb^{3+}, Tm^{3+} UCNPs in the PtTFPP-PS OSP, and the oxygen sensing performance of the UC OSP was evaluated based on both PL lifetime and intensity-based Stern-Vomer diagram in water and air. The sensing parameters were compared with the condition when the sensing molecules were directly excited with 410 nm photons. It was shown for the first time that the UCNPs-PS alone exhibit oxygen sensitivity, and it was boosted more than 10-time by introducing the PtTFPP OSP in the matrix with a 68 % energy transfer efficiency. The lifetime-based O_2 measurements were performed in parallel to PL intensity in order to circumvent the photobleaching errors affecting the sensing parameters. It was observed that the lifetime Stern-Volmer slope of the UC OSP for 980 nm indirect excitation photons was comparable to the direct excitation with 410 nm photons and any significant decrease was not observed. In addition, better reversibility was observed in the air than in water, which is attributed to the lower signal-to-noise ratio, and 410 nm photons better than 980 nm photons which are attributed to their different absorbance in water. Stabilities were almost similar in air and water and lower for 980 nm excited UC OSP. The temperature-dependent lifetime experiment revealed the 980 nm-excited UC OSP is more susceptible to variations in temperature which is attributed to its effect on the energy transfer between UCNP and PtTFPP. In the end, the key advantage of the 980 nm excitation was demonstrated by implanting the UC OSP under the chicken skin and a 16.0-time decrease in the skin absorbance and 12.8-time increase in the PL intensity were observed which is important for implantable applications where the signal to noise ratio matters.

Author Contributions

Experiments, figure preparation, and schematic drawing were performed by Javad AmirAhmadi under the direct supervision of Dr Esmaeil Heydari in the Nanophotonic Sensors & Optofluidics Lab at the Kharazmi University to carry out his M.Sc dissertation project. The paper was written by Javad AmirAhmadi, and Dr Esmaeil Heydari and revised by Dr Hossein Zare-Behtash and Professor Gongxun Bai. The UCNPs was provided by Professor Gongxun Bai and Dr Nahid Ghazyani. Dr MohammadHossein Majlesara is the second supervisor of Javad AmirAhmadi.

Conflicts of interest

There are no conflicts to declare.

Notes and references

1 X. D. Wang and O. S. Wolfbeis, *Chem Soc Rev*, 2014, **43**, 3666-3761.https://doi.org/10.1039/c4cs00039k
2 Amao and Yutaka, *Microchimica Acta*, 2003, **143**, 1-12.https://doi.org/10.1007/s00604-003-0037-x
3 M. I. Stich, L. H. Fischer and O. S. Wolfbeis, *Chem Soc Rev*, 2010, **39**, 3102-3114.https://doi.org/10.1039/b909635n
4 Q. A. Acton, *Boron compounds—advances in research and application: 2012 Edition*, ScholarlyEditions, 2012.
5 X. Wei and B. Gu, *Optical imaging in human disease and biological research*, Springer Singapore, 2021.
6 J. N. Demas, B. A. DeGraff and W. Xu, *Analytical Chemistry*, 1995, **67**, 1377-1380.https://doi.org/10.1021/ac00104a012
7 Y. Luo, Y. Zhang, M. Lang, X. Guo, T. Xia, T. Wang, H. Jia and L. Zhu, *Frontiers of Environmental Science & Engineering*, 2021, **15**, 96.https://doi.org/10.1007/s11783-020-1340-z
8 D. Papkovsky, A. V. Zhdanov, A. Fercher, R. Dmitriev and J. Hynes, *Phosphorescent Oxygen-Sensitive Probes*, Springer Basel, 2012.
9 C. L. McNeil and E. A. D'Asaro, *Limnology and Oceanography: Methods*, 2014, **12**, 139-154.https://doi.org/10.4319/lom.2014.12.139
10 N. M. Idris, M. K. Gnanasammandhan, J. Zhang, P. C. Ho, R. Mahendran and Y. Zhang, *Nature Medicine*, 2012, **18**, 1580-1585.https://doi.org/10.1038/nm.2933
11 X. Liu, H. Chen, Y. Wang, Y. Si, H. Zhang, X. Li, Z. Zhang, B. Yan, S. Jiang, F. Wang, S. Weng, W. Xu, D. Zhao, J. Zhang and F. Zhang, *Nature Communications*, 2021, **12**, 5662.https://doi.org/10.1038/s41467-021-25993-7
12 A. N. Bashkatov, E. A. Genina, V. I. Kochubey and V. V. Tuchin, *Journal of Physics D: Applied Physics*, 2005, **38**, 2543-2555.https://doi.org/10.1088/0022-3727/38/15/004
13 D. E. Achatz, R. J. Meier, L. H. Fischer and O. S. Wolfbeis, *Angew Chem Int Ed Engl*, 2011, **50**, 260-263.https://doi.org/10.1002/anie.201004902
14 F. Auzel, *Chem Rev*, 2004, **104**, 139-173.https://doi.org/10.1021/cr020357g
15 J.-C. G. Bünzli, S. Comby, A.-S. Chauvin and C. D. B. Vandevyver, *Journal of Rare Earths*, 2007, **25**, 257-274.https://doi.org/10.1016/s1002-0721(07)60420-7
16 J. Shen, L. D. Sun and C. H. Yan, *Dalton Trans*, 2008DOI, 5687-5697.https://doi.org/10.1039/b805306e
17 F. Auzel, *Comptes Rendus Hebdomadaires Des Seances De L Academie Des Sciences Serie B*, 1966, **263**, 819-&
18 V. Ovsyankin and P. Feofilov, *Soviet Journal of Experimental and Theoretical Physics Letters*, 1966, **3**, 322
19 N. Fallahi Chegeni, P. Ijadi Maghsoodi, M. Habibi, B. Zare, H., M. H. Majles Ara and E. Heydari, *Sensors (Basel)*, 2021, **21**.https://doi.org/10.3390/s21196553
20 M. Habibi, P. Bagheri, N. Ghazyani, B. Zare, Hossein and E. Heydari, *Sensors and Actuators A: Physical*, 2021, **326**, 112734.https://doi.org/10.1016/j.sna.2021.112734
21 Y. Luo, L. Zhang, Y. Liu, E. Heydari, L. Chen and G. Bai, *Journal of the American Ceramic Society*, 2022, **105**, 1375-1385.https://doi.org/10.1111/jace.18153
22 A. de Bettencourt-Dias, *Dalton Trans*, 2007DOI, 2229-2241.https://doi.org/10.1039/b702341c
23 S. V. Eliseeva and J. C. Bunzli, *Chem Soc Rev*, 2010, **39**, 189-227.https://doi.org/10.1039/b905604c
24 S. Gai, C. Li, P. Yang and J. Lin, *Chem Rev*, 2014, **114**, 2343-2389.https://doi.org/10.1021/cr4001594
25 X. Huang, S. Han, W. Huang and X. Liu, *Chem Soc Rev*, 2013, **42**, 173-201.https://doi.org/10.1039/c2cs35288e
26 Y. Lu, J. Zhao, R. Zhang, Y. Liu, D. Liu, E. M. Goldys, X. Yang, P. Xi, A. Sunna, J. Lu, Y. Shi, R. C. Leif, Y. Huo, J. Shen, J. A. Piper, J. P. Robinson and D. Jin, *Nature Photonics*, 2014, **8**, 32-36.https://doi.org/10.1038/nphoton.2013.322
27 Q. Kuang, X. Wang, Z. Jiang, Z. Xie and L. Zheng, *Accounts of Chemical Research*, 2014, **47**, 308-318.https://doi.org/10.1021/ar400092x
28 H. S. Dong, Ling,Dong Wang, Ye,Fu Xiao, Jia,Wen Tu, Datao Chen, Xueyuan Yan, Chun,Hua, *Journal of Materials Chemistry C*, 2016, **4**, 4186-4192.https://doi.org/10.1039/C6TC00413J
29 H. Dong, L. D. Sun and C. H. Yan, *Nanoscale*, 2013, **5**, 5703-5714.https://doi.org/10.1039/c3nr34069d
30 J. L. Bergstrand, Q. Huang, B. Peng, X. Wurth, C. Resch,Genger, U. Zhan, Q. Widengren, J. Agren, H. Liu, H., *Nanoscale*, 2019, **11**, 4959-4969.https://doi.org/10.1039/c8nr10332a
31 A. F. M. García-Flores, J. S. Garcia, D. J. Martínez, E. D. Cornaglia, P. S. Lesseux, G. G. Ribeiro, R. A. Urbano, R. R. Rettori, C., *Physical Review B*, 2017, **96**, 165430.https://doi.org/10.1103/PhysRevB.96.165430
32 S. V. Gaponenko and H. V. Demir, *Energy transfer processes,Applied Nanophotonics*, Cambridge University Press, Cambridge, 2018.
33 H. Dong, L. D. Sun and C. H. Yan, *Chem Soc Rev*, 2015, **44**, 1608-1634.https://doi.org/10.1039/c4cs00188e
34 H. W. Li, X. Huang, D. Chen, G., *Nanotechnology*, 2020, **31**, 072001.https://doi.org/10.1088/1361-6528/ab4f36
35 M. S. T. Meijer, V. S. Hilbers, M. F. Kieltyka, R. E. Brouwer, A. M. Natile, M. M. Bonnet, S., *Langmuir*, 2019, **35**, 12079-12090.https://doi.org/10.1021/acs.langmuir.9b01318
36 K. H. Presley, J. Cheong, S. Tilley, R. Collins, J. Viapiano, M. Lannutti, J., *Mater Sci Eng C Mater Biol Appl*, 2017, **70**, 76-84.https://doi.org/10.1016/j.msec.2016.08.056
37 E. Ruggiero, A. Habtemariam, L. Yate, J. C. Mareque-Rivas and L. Salassa, *Chem Commun (Camb)*, 2014, **50**, 1715-1718.https://doi.org/10.1039/c3cc47601d
38 R. Deng, J. Wang, R. Chen, W. Huang and X. Liu, *Journal of the American Chemical Society*, 2016, **138**, 15972-15979.https://doi.org/10.1021/jacs.6b09349
39 T. Chen, Y. Shang, Y. Zhu, S. Hao and C. Yang, *ACS Applied Materials & Interfaces*, 2022, **14**, 19826-19835.https://doi.org/10.1021/acsami.2c00604

40 M. Quaranta, S. M. Borisov and I. Klimant, *Bioanal Rev*, 2012, **4**, 115-157.https://doi.org/10.1007/s12566-012-0032-y
41 M. Tou, Y. Mei, S. Bai, Z. Luo, Y. Zhang and Z. Li, DOI.https://doi.org/10.1039/c5nr06806a
42 C. Li, F. Wang, J. Zhu and J. C. Yu, *Applied Catalysis B: Environmental*, 2010, **100**, 433-439.https://doi.org/10.1016/j.apcatb.2010.08.017
43 W. Huang, M. Ding, H. Huang, C. Jiang, Y. Song, Y. Ni, C. Lu and Z. Xu, *Materials Research Bulletin*, 2013, **48**, 300-304.https://doi.org/10.1016/j.materresbull.2012.10.031
44 Y. Zhang, B. Chen, S. Xu, X. Li, J. Zhang, J. Sun, H. Zheng, L. Tong, G. Sui, H. Zhong, H. Xia and R. Hua, *Scientific Reports*, 2017, **7**, 11849.https://doi.org/10.1038/s41598-017-11897-4
45 H. Qin, D. Wu, J. Sathian, X. Xie, M. Ryan and F. Xie, *Scientific Reports*, 2018, **8**, 12683.https://doi.org/10.1038/s41598-018-30983-9
46 N. J. Bhalla, P. Formisano, N. Estrela, P., *Essays Biochem*, 2016, **60**, 1-8.https://doi.org/10.1042/EBC20150001
47 L. C. W. Chen, E. Tai, C. S. Chiu, Y. C. Li, C. W. Lin, Y. R. Lee, T. H. Huang, C. W. Chen, J. C. Chen, W. L., *Biosens Bioelectron*, 2020, **155**, 112111.https://doi.org/10.1016/j.bios.2020.112111
48 F. Kaboli, N. Ghazyani, M. Riahi, B. Zare, Hossein, M. H. Majles Ara and E. Heydari, *ACS Applied Nano Materials*, 2019, **2**, 3590-3596.https://doi.org/10.1021/acsanm.9b00549
49 C. Li, F. Wang, J. Zhu and J. C. Yu, *Applied Catalysis B: Environmental*, 2010, **100**, 433-439.https://doi.org/10.1016/j.apcatb.2010.08.017
50 W. Zhang, J. Li, H. Lei and B. Li, *Opt Express*, 2020, **28**, 12450-12459.https://doi.org/10.1364/OE.386601